Flow-through electro-Fenton using nanoconfined Fe-Mn bimetallic oxides: Ionization potential-dependent micropollutants degradation mechanism

Dongli Guo [a], Yi Wang [b,*], Ping Lu [c], Jie Liu [d], Yanbiao Liu [a,e,**]

[a] College of Environmental Science and Engineering, Donghua University, Shanghai 201620, China
[b] Laboratory of Environmental Technology, INET, Tsinghua University, Beijing 100084, China
[c] Research Center for Analysis and Measurement, Donghua University, Shanghai 201620, China
[d] Department of Military Facilities, Army Logistics University, Chongqing 401331, China
[e] Shanghai Institute of Pollution Control and Ecological Security, 1239 Siping Road, Shanghai 200092, íChina

A B S T R A C T

Herein, we present a flow-through electro-Fenton system for highly efficient and selective degradation of organic contaminants. The essential to this design was a functional nanohybrid filter cathode consisting of an electro-active carbon nanotube (CNT) filter functionalized with bimetallic Fe/Mn oxide nanoparticles under nano-confinement. Results suggested that the nanoconfined Fe/Mn-in-CNT filter exhibited a much higher organic degradation kinetics (1.65 times) relative to its unconfinement counterpart (Fe/Mn-out-CNT). Singlet oxygen was the primary reactive oxygen species in the Fe/Mn-in-CNT-based system, in sharp contrast with the hydroxyl radical-mediated pathway in the Fe/Mn-out-CNT-based system. The efficacy was closely correlated with the ionization potential of target organic molecules, with preferentially oxidized organics with the electron-donating ability. Both experimental evidences and theoretical results collectively revealed the superior performance associated with the synergistic effects among Fe, Mn, CNT, and electric field in the nanoconfined system.

1. Introduction

The issues of anthropogenic water pollution and scarcity of clean water are major global challenges [1–3]. Advanced oxidation processes (AOPs) are recognized approaches that can effectively decontaminate diverse aqueous organic contaminants because the generated reactive oxygen species (ROS) possess strong oxidative capabilities for mineralizing organic molecules [4,5]. Among them, electro-Fenton has been widely adopted for highly efficient destruction of diverse refractory organic pollutants [6,7]. During this process, H_2O_2 and Fe^{2+} are continuously generated in-situ by cathodic reduction of O_2 and Fe^{3+}, accompanied by the formation of hydroxyl radicals ($HO^{\bullet}$) [8]. Unfortunately, the large-scale implementation of classic heterogeneous electro-Fenton technology is limited by poor ROS utilization efficiency due to mass transfer limitations and radicals quenching by coexisting water constituents [9].

Recently, nanoconfined catalysis has emerged as a viable strategy to improve the ROS utilization efficiency [10] by restricting the desirable reaction occurred within nano-confined space [11]. In this case, the diffusion distance of aqueous organic molecules toward active catalysis sites was substantially decreased. Therefore, a significant improvement of short-lived radical availability could be envisaged. Various types of nanoreactors have been explored to perform space-confined reactions [12], such as one-dimensional nanotubular channels [13], interlayer spaces between two-dimensional nanosheets [11], and nanocavities within core-shell structures [14]. Of these, one-dimensional carbon nanotubes (CNTs) have gained great attention owing to their desirable physiochemical attributes [15]. For example, Fe_2O_3 nanoparticles confined within CNT showed remarkably higher methylene blue degradation activity (22.5 times faster) than its nonconfined analog [16]. Besides, CNT-based nanoconfined catalysts have also demonstrated multiple new mechanisms, such as selective oxidation using $^1O_2$ [13], high-valent metal-oxo species [17] or direct electron transfer process [18]. Despite nanoconfinement catalysts are attractive for water treatment, their practical implementation is significantly hindered by the limitations associated with post-separation and recovery from reaction solution in conventional batch reactors.

To avoid such negative effect on water safety, it is highly desirable to

---

design supported nanoscale Fenton catalysts under nanoconfinement [19]. We have previously confined Fe_2O_3 nanoparticles inside CNT to form Fe_2O_3-in-CNT membrane electrode for catalytic removal of micropollutants [13]. Comparison to conventional batch reactor, mass transfer could be significantly improved due to convective transport in the flow-through configuration [20]. Besides, the post-separation of nanoscale catalysts was well addressed in such design. To the best of our knowledge, only very rare reports are available on the rational design of flow-through membrane electrode based on nanoconfined catalysts.

Various transition metals such as Co, Ni, Fe and Mn were capable to serve as effective catalysts for Fenton chemistry [21]. However, the wide application of Co and Ni are hindered by their high toxicity [22]. Alternatively, the development of Fe- and Mn-based catalysts are widely pursued owing to their environmentally benignity and abundant reserves [23]. Moreover, the synergistic effect between Mn and Fe in binary oxides has been pursued to outperform their sole counterparts. For example, a Fe-Mn-O nanosheets/carbon nanocomposite exhibited much higher activity toward the degradation of tetracycline, which achieved a reaction rate of 3.9 and 2.4-fold higher than those of individual MnO_2 and FeOOH [24].

Herein, we rationally designed and demonstrated a flow-through electro-Fenton system enabled selective oxidation of micropollutants with ionization potential (IP) lower than 9.0 eV. The essential to this design was an electroactive nanohybrid filter composed of CNT networks functionalized with nanoconfined Fe/Mn nanocatalysts. To do this, we firstly synthesized CNT encapsulated Fe/Mn oxides (Fe/Mn-in-CNT) *via* a wet chemistry protocol. The physicochemical properties of the nanohybrid filters were systematically investigated based on various advanced characterization techniques. The underlying mechanism toward organic degradation was proposed based on theoretical calculations and experimental observations. The advantage of nanoconfined catalysis was quantitatively exemplified by comparing the system efficacy with a non-confined counterpart (Fe/Mn-out-CNT). The relationship between ionization potential (IP) and corresponding degradation kinetics of organic molecules was established to evaluate their selective catalytic activity. Finally, the potential practical applications of the proposed technology were further explored by challenging with diverse refractory micropollutants. The outcome of this study is dedicated to provide a promising strategy for water decontamination by combining state-of-the-art nanoconfined catalysis, Fenton chemistry and microfiltration technology.

2. Materials and methods

2.1. Preparation of confined and unconfined nanohybrid filters

The Fe/Mn-in/out-CNT samples were prepared using a wet-chemistry protocol with modifications [25]. Those Fe/Mn oxide nanoparticles were drawn into the CNT channels utilizing capillary force of nanotube aided by ultrasonic and stirring treatment, by which the obtained sample was denoted as Fe/Mn-in-CNT. As comparison, Fe/Mn oxide nanoparticles with a similar loading were loaded onto the CNT outer surface to obtain the Fe/Mn-out-CNT. The actual loading amount of Fe and Mn for the Fe/Mn-out-CNT and Fe/Mn-in-CNT samples was listed in Table S1. Nanohybrid filters can be fabricated by vacuum filtration of the dispersion solution of Fe/Mn-in/out-CNT samples onto a commercial polytetrafluoroethylene membrane (Fig. S1) [26].

2.2. Electrochemical filtration experiments

Electrochemical filtration tests were implemented using an electrochemistry-modified Whatman filtration casing [27]. The as-prepared nanohybrid filter was utilized as cathode and a perforated titanium sheet was used as anode. A 0.022 mM BPA (equivalent to 5.0 mg/L BPA) was chosen based on their reported levels detected in a landfill leachate (~3.5 mg/L) [28,29]. Two operational modes

(recirculated filtration and batch) were performed for comparison. In a typical recirculated filtration process, 0.022 mM BPA (50 mL) with O_2-saturated 10 mM Na_2SO_4 solution were challenged the filtration system in the recirculating filtration mode. Flow rate was controlled by a Longer L100–1S-1peristaltic pump (China). Applied voltage was provided by a DH1766A-1 DC power supply. For the batch mode, the BPA removal test were performed in a beaker where the Fe/Mn-in-CNT filter and Ti sheet were used as cathode and anode, respectively. Effluent (0.5 mL) was collected at pre-determined time interval to monitor the evolution of BPA concentration. 1.0 mM NaOH or HCl was used to adjust solution pH. Triplicate experiments were conducted to ensure reproducibility.

2.3. Characterization

High-resolution transmission electron microscopy (HRTEM) images were captured on a Talos F200S field emission transmission electron microscope equipped with a Bruker XFlash 5010 energy-dispersive detector. The morphologies and cross-sectional view of the filters were observed by a Hitachi S-4800 field emission scanning electron microscope (FESEM, Japan). Surface chemistry and phase structure of the nanohybrid filters were examined by X-ray photoelectron spectroscopy (XPS, Thermo Fisher Scientific Escalab 250Xi, USA) and X-ray diffraction (XRD, Rigaku SmartLab SE, Japan). The magnetic property was examined on a vibration sample magnetometer (VSM, Lake Shore, USA) at room temperature. Brunauere-Emmette-Teller (BET) specific areas of nanohybrid filters were obtained using a Quantachrome Autosorb iQc analyzer (USA). Zeta potential was recorded by a particle size/zeta potential analyzer (Brookhaven 90Plus, USA). Electrochemical tests were performed on a CHI-660D electrochemical workstation in a three-electrode configuration.

2.4. Analytical methods

The concentration of BPA, 4-chlorophenol (4-CP), benzoic acid (BA), phenol, and *p*-nitrophenol (PNP) was analyzed by using a high-performance liquid chromatography (HPLC, Shimadzu LC-16, Japan) equipped with a ShimNex CS C18 column (5 μm, 4.6 ×250 mm). Details on the analytical methods were listed in Table S2. BPA degradation intermediates were identified by using an Agilent LC1290-QQQ-6470 liquid chromatography-mass spectrometry system (LC-MS, Singapore). The concentration of H_2O_2 was measured by a spectrophotometric potassium iodide protocol (Text S1). Leachable Mn and Fe ions were examined by iCAP-Q inductively coupled plasma mass spectrometry (ICP-MS, Thermo Scientific).

Electron paramagnetic resonance (EPR, EMXnano, Bruker) was employed to verify the reactive species, with 2,2,6,6-tetramethylpiperidine (TEMP) and 5,5-dimethyl-1-pyrrolidine-N-oxide (DMPO) served as spin-trapping reagents to detected the adducts of TEMP-$^1O_2$ and DMPO-HO$^{\bullet}$, respectively. The concentration of total organic carbon (TOC) was determined using a TOC analyzer (TOC-L CPH, SHIMADZU, Japan). Toxicity of BPA and its degradation intermediates were assessed by quantitative structure-activity relationship (QSAR) analysis utilizing the Toxicity Estimation Software Tool (T.E.S.T.).

2.5. Theoretical calculations

Density functional theory (DFT) simulation was conducted by Vienna Ab-initio Simulation Package software [30] with the projector augmented wave method [31]. The convergence value of energy was set as 10^{-5} eV, and the convergence value of force on each atom was 0.05 eV/Å. K-points were 3 * 3 * 2. The cut-off energy was 400 eV. The adsorption energy was calculated according to Eq. (1),

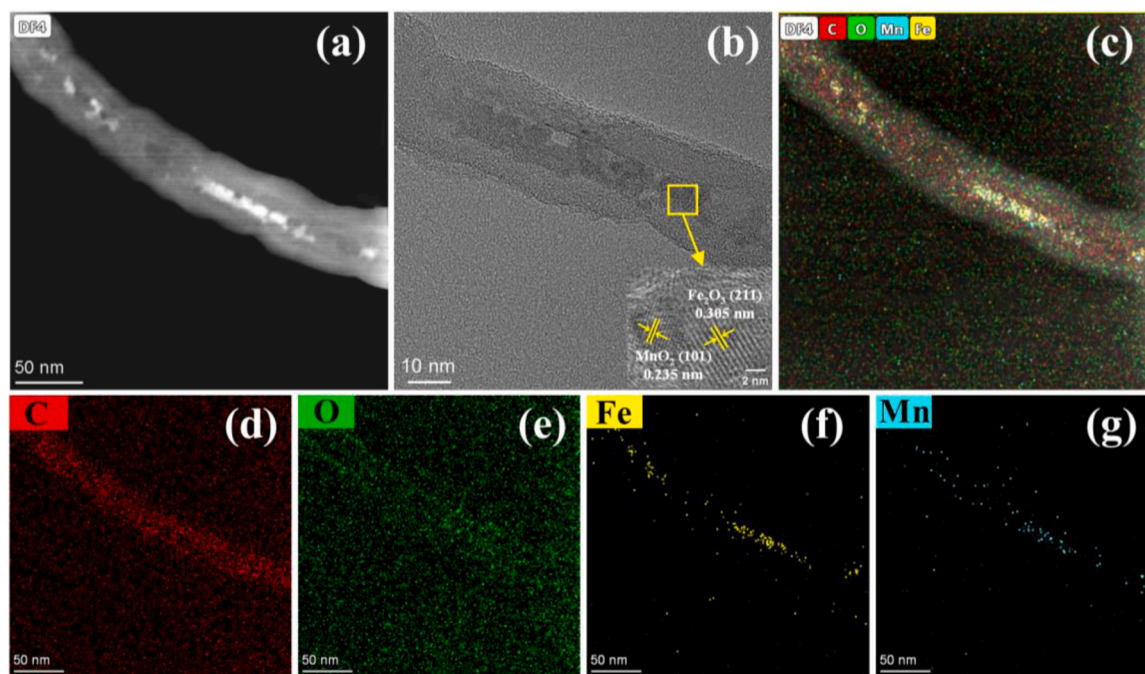$$E_{ads} = E_{(catalysts+H_2O_2)} - E_{catalysts} - E_{H_2O_2} \tag{1}$$

Fig. 1. (a) Representative HADDF-STEM image of Fe/Mn-in-CNT filter, (b) HRTEM image of Fe/Mn oxides nanoparticles, (c-g) elemental mapping images of the Fe/Mn-in-CNT filter.

where E_{ads} was the adsorption energy, $E_{(catalysts+H_2O_2)}$ was the total energy after the adsorbates were adsorbed on catalysts, $E_{catalysts}$ was the energy of the sole catalysts, and $E_{H_2O_2}$ was the molecular energy of H_2O_2.

3. Results and discussion

3.1. Filter characterization

The Fe/Mn-in/out-CNT composites were synthesized *via* a wet chemistry route with modifications [25]. TEM image revealed that nanoscale Fe/Mn oxides particles were located outside the CNT for the Fe/Mn-out-CNT sample. High-resolution TEM (HRTEM) image showed that the *d*-spacings of 0.227 and 0.305 nm, belong to the (113) and (102) facets of Fe_2O_3 and MnO_2, respectively (Fig. S2). For the Fe/Mn-in-CNT counterpart, Fe/Mn oxide particles were confined within the nanoscale tubular channels of CNT (Fig. 1a). These nanoconfined particles exhibited typical lattice stripe spacings of 0.305 and 0.235 nm, corresponding to (211) and (101) planes of Fe_2O_3 and MnO_2, respectively, as suggested by the HRTEM image (Fig. 1b). Elemental mapping data confirmed the co-existence of Fe, Mn, O, and C (Fig. 1c-g). The size-distribution histograms of Fe/Mn oxides nanoparticles in both samples (Fig. S3) showed the average size to be 3.6 ± 0.9 nm (Fe/Mn-in-CNT) and 5.5 ± 1.3 nm (Fe/Mn-out-CNT). As shown in Fig. S4, these 1D CNT intertwined each other and no apparent change can be observed after the loading of Fe/Mn oxides. Cross-sectional view of the prepared Fe/Mn-in-CNT filter suggested a typical thickness of 49.3 ± 12.6 μm (Fig. S5).

Crystalline structures of Fe/Mn-out-CNT and Fe/Mn-in-CNT filters were further evident by XRD. As displayed in Fig. 2a, all diffraction peaks were identical to the mixed phases of ε-MnO_2 (JCPDS No. 30–8020) and α-Fe_2O_3 (JCPDS No. 33–0664) for the Fe/Mn-out-CNT and Fe/Mn-in-CNT filters, respectively. The negligible magnetic response of Fe/Mn-out-CNT and Fe/Mn-in-CNT samples excluded the potential formation of $MnFe_2O_4$ (Fig. S6). BET surface area of the Fe/Mn-in-CNT filter was 167.8 m^2/g (Fig. S7), slightly higher than that of Fe/Mn-out-CNT filter of 132.7 m^2/g, possibly due to the opening of CNT tips [32]. Elemental compositions and chemical states of

Fe/Mn-in/out-CNT samples were studied by XPS technique. The XPS survey pattern in Fig. 2b showed the constituents C, O of CNT and C, O, Mn, Fe of Fe/Mn-in-CNT and Fe/Mn-out-CNT. The O 1 s spectra (Fig. 2c) could be deconvoluted into three peaks attributed to surface lattice oxygen (O_L, 529.8 eV), due to oxygen atoms bound to metals, oxygen in surface hydroxyl groups (O_{HO}, 531.4 eV), and oxygen in adsorbed water (O_w, 533.0 eV) on the catalyst [33]. XPS Fe 2p spectra (Fig. 2d) could be deconvoluted into two overlapping peaks with binding energy of 711.8 eV and 710.5 eV, which was attributed to Fe(III) and Fe(II) [34], respectively. Similarly, the Mn 2p spectra (Fig. 2e) could be deconvoluted into two peaks with binding energies of 642.9 eV and 641.7 eV associated with Mn(IV) and Mn(III) [35], respectively. Specifically, the Fe/Mn-in-CNT showed similar Fe(III) amount to that of Fe/Mn-out-CNT, and 1.5 times higher Mn(IV) amount than that of Fe/Mn-out-CNT (56.5% *vs* 37.2%) (Fig. 2d-e). These evidences collectively suggested that the Fe/Mn-out-CNT and Fe/Mn-in-CNT hybrid filters were successfully fabricated.

Cyclic voltammetry (CV) curves of the Fe/Mn-in-CNT filter in N_2/O_2-saturated 0.1 M Na_2SO_4 solution were comparatively measured to evaluate its electrochemical activity. As shown in Fig. 3a, the CV curve of Fe/Mn-in-CNT filter showed a distinct ORR peak at a potential of -0.308 V *vs.* Ag/AgCl in O_2-saturated solution, indicating the occurrence 2e⁻ ORR. Similar phenomenon was also observed for the Fe/Mn-out-CNT filter (Fig. S8). In addition, electrochemical impedance spectroscopy (EIS) measurements were performed to analyze the electron transport properties of the filters. Nyquist plots of Fe/Mn-out-CNT filter and Fe/Mn-in-CNT filter electrodes were shown in Fig. 3b. Data were simulated in terms of the model circuit (Fig. S9). The charge transfer resistance (R_{ct}) value of Fe/Mn-in-CNT filter (11.8 Ω) was much lower than that of Fe/Mn-out-CNT filter (44. 1 Ω), indicating a decreased resistance of electron transfer during electrochemical filtration [36].

3.2. Water decontamination performance using the nanohybrid filters

The performance of as-fabricated nanohybrid filters were evaluated using BPA as a representative emerging contaminant. To exclude any contribution from physical adsorption on the BPA removal, all filters
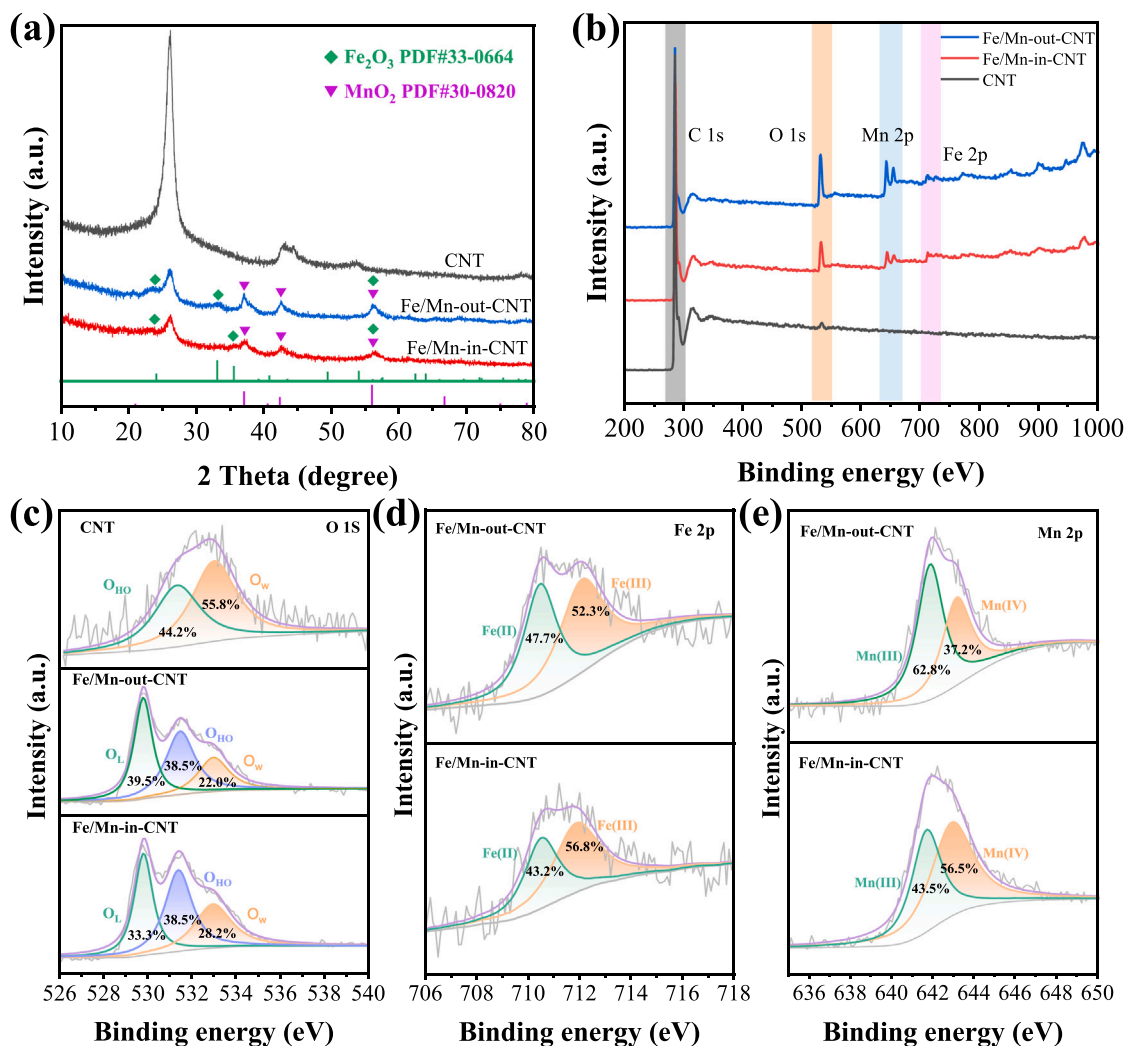
Fig. 2. (a) XRD patterns, (b) XPS spectra, and the deconvolution of XPS (c) O 1 s, (d) Fe 2p, and (e) Mn 2p spectra of Fe/Mn-in-CNT and Fe/Mn-out-CNT samples.
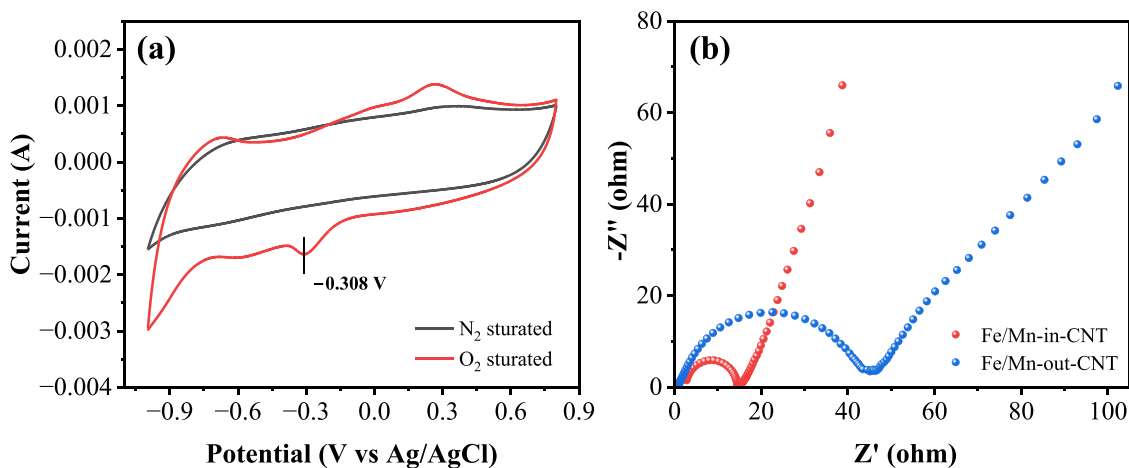

Fig. 3. (a) Cyclic voltammograms of the Fe/Mn-in-CNT filter in 0.1 M Na_2SO_4 (N_2- and O_2-saturated) with a scan rate at 10 mV/s. (b) Nyquist plots of the Fe/Mn-in-CNT and Fe/Mn-out-CNT filters.

were achieved sorption saturation by passing through 180 mL of BPA solution (0.022 mM) in the absence of electric field. As exhibited in Fig. 4a, H_2O_2 alone could not effectively oxidize BPA with using pristine CNT filter as cathode, as the degradation efficiency and *k* value were

only 38.9% and 0.022 min^{-1}, respectively. After introducing the Fe/Mn catalysts, the BPA removal efficiencies using varying filters followed the order of Fe/Mn-in-CNT (99.5%) > Fe/Mn-out-CNT (70.8%) > Mn-in-CNT (62.8%) > Fe-in-CNT (50.4%) > CNT (38.9%). As compared with
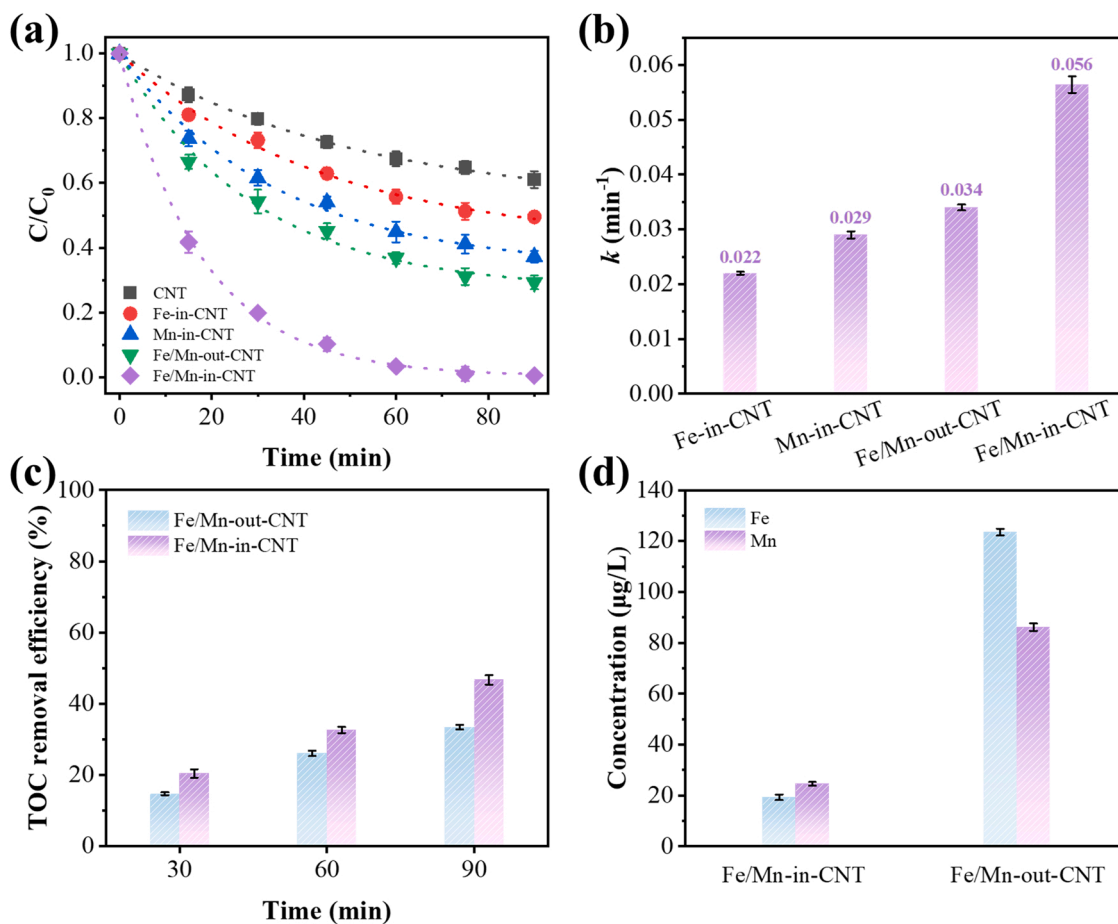
Fig. 4. (a) Kinetics of BPA degradation in different systems. (b) histogram of degradation kinetic constant values of different systems. (c) TOC removal efficiency during BPA degradation in both Fe/Mn-in-CNT and Fe/Mn-out-CNT-based systems. (d) the concentration of leaching Fe and Mn in solution reaction in Fe/Mn-in-CNT and Fe/Mn-out-CNT-based systems. Experimental conditions: $[BPA]_0 = 0.022$ mM, $[DO]_0 = 37.6 \pm 1.2$ mg/L, $[Na_2SO_4] = 10$ mM, voltage $= -3.0$ V, $[pH]_0 = 6.8$, and flow rate $= 1.5$ mL/min.

Fe-in-CNT filter, the introduction of Mn obviously enhanced the BPA degradation kinetics (0.022 min^{-1} *vs* 0.056 min^{-1}), suggesting the synergistic effect of these bimetallic nanoparticles (Fig. 4b). Noticeably, the BPA degradation kinetics in the Fe/Mn-in-CNT-based electro-Fenton system (0.056 min^{-1}) was 1.65-fold faster than that of the Fe/Mn-out-CNT-based system (0.034 min^{-1}). Similar results were also obtained in TOC tests (Fig. 4c), with Fe/Mn-in-CNT demonstrating an improved mineralization efficiency (46.7%) within 90 min compared with that of Fe/Mn-out-CNT (33.4%). Besides, the homogeneous electro-Fenton, heterogeneous Fenton using externally spiked H_2O_2, and direct anodic oxidation process all exhibited significantly lower BPA degradation kinetics compared with the Fe/Mn-in-CNT-based system (Fig. S10).

The catalyst stability was improved as well in the nanoconfined configuration [37]. As shown in Fig. 4d, the leachable Fe and Mn ions in the Fe/Mn-in-CNT-based system was only 19.3 µg/L and 24.6 µg/L, respectively, which was 6.4 and 3.5 times lower than those of Fe/Mn-out-CNT-based system (*i.e.*, 123.5 µg/L and 86.2 µg/L). In addition, the mass transfer rate constant (k_m) of Fe/Mn-in-CNT-based system (8.2×10^{-4} cm/s) was also 1.5 times higher than that of Fe/Mn-out-CNT-based system (5.3×10^{-4} cm/s) (Text S1). All these results quantitatively exemplified the advantages of the nanoconfined design.

3.3. Mechanism study

3.3.1. Generation of reactive species

EPR and ROS quenching experiments were collectively employed to investigate the mechanism of the flow-through electro-Fenton systems. First, EPR experiments were performed to verify the dominant active species. No traceable signal was observed for the CNT alone and Fe/Mn-in-CNT-based systems, while a typical quadruple peak signal with an intensity of 1:2:2:1 spectrum ascribed to DMPO-HO• adduct was obtained for the Fe/Mn-out-CNT-based system (Fig. 5a). In addition, a representative triplet peak signal of TEMP-$^1O_2$ adduct was observed in the Fe/Mn-in-CNT-based system (Fig. 5b). Noticeably, this was not detected in both Fe/Mn-out-CNT and CNT systems. The results suggested that HO• was the primary oxidative species in the Fe/Mn-out-CNT-based system, while $^1O_2$ was the dominant ROS in the Fe/Mn-in-CNT-based system, which would be further verified by using quenching experiments.

A series ROS quenching tests were carried out to identify the dominant ROS in Fe/Mn-in/out-CNT-based systems. The results of quenching experiments with different radical scavengers (*tert*-butyl alcohol (TBA) for eliminating HO•, furfuryl alcohol (FFA) for $^1O_2$, methyl phenyl sulfoxide (PMSO) for high-valent metal-oxo species) indicated the generation of HO• and $^1O_2$ in the Fe/Mn-out-CNT and Fe/Mn-in-CNT-based system, respectively, which were consistent with the results of EPR test (Fig. 5c). In addition, *p*-benzoquinone (*p*-BQ) addition caused no obvious suppression in Fe/Mn-out-CNT-based system, indicating $O_2^{\bullet-}$ were not generated. Instead, addition of 50 mM *p*-BQ impressively inhibited the BPA degradation in the Fe/Mn-in-CNT-based system, indicating that $O_2^{\bullet-}$ was involved in $^1O_2$ generation. As for the $^1O_2$ generation, it might be resulted from the recombination or direct oxidation of $O_2^{\bullet-}$ [16], which could be generated over the Fe/Mn oxides
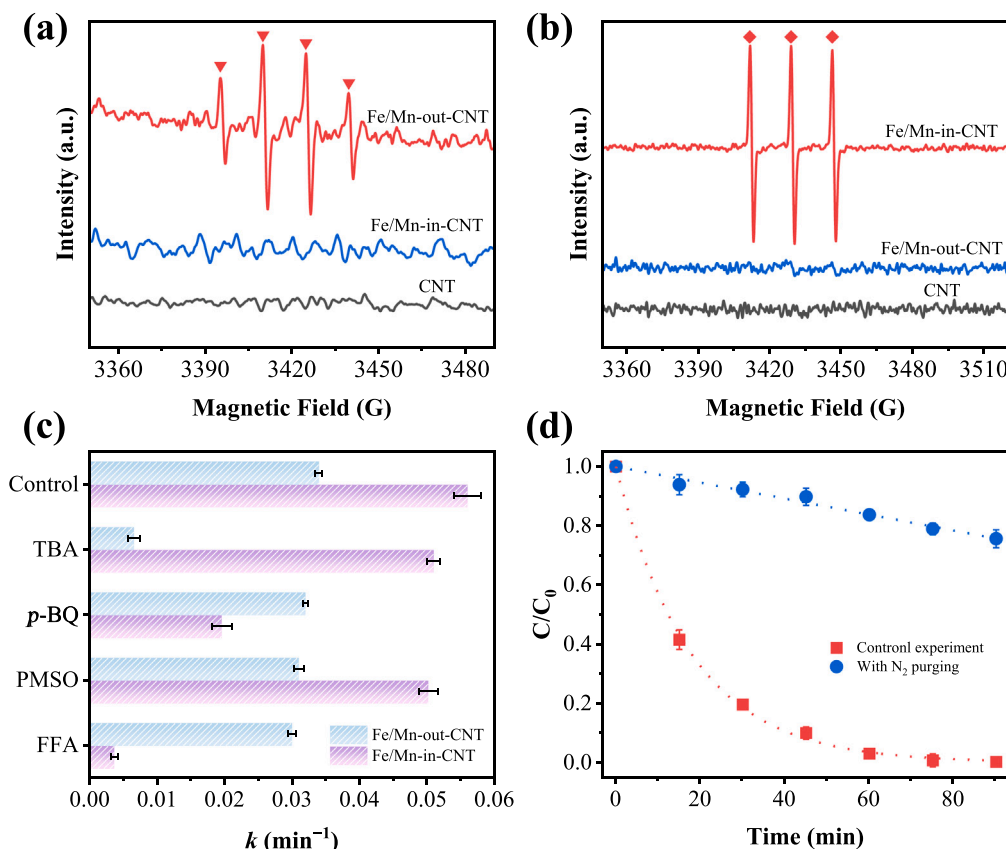
Fig. 5. Identification of ROS: EPR spectra for (a) DMPO-HO$^{\bullet}$ ▼ and (b) TEMP-^{1}O$_2$ ◆. (c) effects of different radical scavengers on BPA degradation kinetics. (d) effect of dissolved oxygen on the degradation of BPA in the Fe/Mn-in-CNT-based system. Experimental conditions: $[p\text{-BQ}]_0 = 50$ mM, $[\text{PMSO}]_0 = 5.0$ mM, $[\text{TBA}]_0 = [L\text{-histidine}]_0 = 100$ mM, $[\text{BPA}]_0 = 0.022$ mM, $[\text{DO}]_0 = 37.6 \pm 1.2$ mg/L, $[\text{Na}_2\text{SO}_4] = 10$ mM, voltage $= -3.0$ V, $[\text{pH}]_0 = 6.8$, and flow rate $= 1.5$ mL/min.
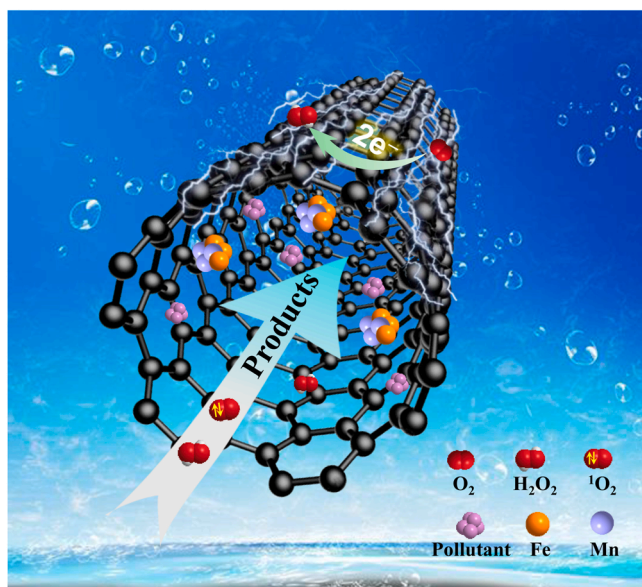

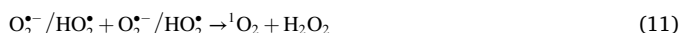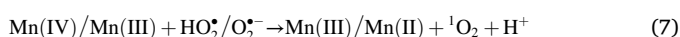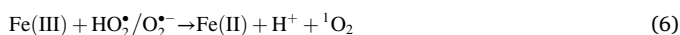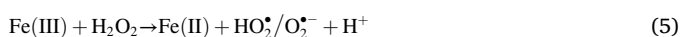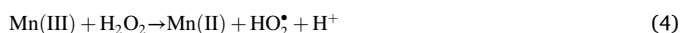**Fig. 6.** Mechanism illustration of pollutants degradation in Fe/Mn-in-CNT-based system.

[38]. In addition, when the reaction solution was saturated with N$_2$ instead of O$_2$, a rather limited BPA degradation efficiency of 24.3% was observed (Fig. 5d). This suggested that O$_2$ was indispensable for the H$_2$O$_2$ generation *via* 2e$^-$ ORR pathway [39].
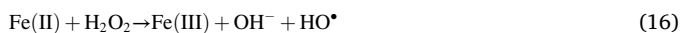
3.3.2. Proposed mechanism

Considering the different ratios of Fe(III) and Fe(II), Mn(IV) and Mn (III) might contribute to the degradation performance of BPA, we tuned the ratios of Fe(III)/Fe(II) and Mn(VI)/Mn(III) for the both samples by adjusting the mass ratio of Fe and Mn, as evidenced by the XPS results (Fig. S11 and Table S3). As shown in Fig. S12, the degradation performance of BPA in the Fe/Mn-in-CNT-based system was always superior to that in the Fe/Mn-out-CNT-based system, suggesting the nanoconfinement effect played a dominant role in dictating the catalytic reactivity. Furthermore, the Fe and Mn content of exhausted Fe/Mn-out-CNT and Fe/Mn-in-CNT filters were analyzed *via* XPS spectroscopy to unveil the possible reaction mechanism. As shown in Fig. S13, a new peak at 641.3 eV emerged in Mn 2p spectra of Fe/Mn-out-CNT and Fe/Mn-in-CNT filters, which could be ascribed to Mn(II). This suggested that part of Mn(III) and Mn(IV) were reduced to Mn(II). For the Fe/Mn-in-CNT filter, the ratio of Fe(II)/Fe(III) showed negligible changes after reaction, indicating that Mn was considered as the main catalytic active site for H$_2$O$_2$ activation [40]. By contrast, the proportion of Fe(II) reduced from 47.8% to 38.6% for the Fe/Mn-out-CNT filter, indicating the synergistic effect of Mn and Fe is attributed to the facilitated cycling of Mn(II)/Mn(III)/Mn(IV) and Fe(III)/Fe(II) pairs [41].

Based on these collective investigations and analyses, ^{1}O$_2$ played a primary role in the degradation of BPA in the Fe/Mn-in-CNT-based system, while HO$^{\bullet}$ was main ROS in the Fe/Mn-out-CNT-based system. For Fe/Mn-in-CNT-based system (Fig. 6), H$_2$O$_2$ was first generated through ORR on the cathode (Eq. (2)), followed by O$_2^{\bullet-}$ or HO$_2^{\bullet}$ accumulation chiefly by the subsequent oxidation of H$_2$O$_2$ in the Fe/Mn-in-CNT (Eqs. (3)–(5)). Benefiting from the continuous production of H$_2$O$_2$ and HO$_2^{\bullet}$/O$_2^{\bullet-}$, the Fe/Mn-in-CNT filter triggered two possible pathways for the ^{1}O$_2$ formation: (i) direct oxidation of HO$_2^{\bullet}$/O$_2^{\bullet-}$ by Fe(III), Mn(IV) or Mn(III) [16,38] (Eqs. (6)–(7)); (ii) recombination of O$_2^{\bullet-}$/HO$_2^{\bullet}$ [42]

(Eqs. (8)–(11)). Noticeably, EPR spectra in the presence of 10 mM p-BQ (quenching agent of $O_2^{\bullet-}$) leaded to a weakened signal intensity of $^1O_2$ (Fig. S14), suggesting $O_2^{\bullet-}$ was the key intermediate for the $^1O_2$ generation. However, no direct evidences for the presence of $O_2^{\bullet-}$ were identified in Fe/Mn-in-CNT-based system according to the EPR tests, which is probably due to the rapid radical recombination in the spatial confinement environment [16]. To further confirm the generation of $^1O_2$ in the Fe/Mn-in-CNT-based system, we determined the EPR spectra by replacing ultrapure water with deuterium oxide (D_2O), since the lifetime of $^1O_2$ in D_2O was significantly higher than that in H_2O [43]. As shown in Fig. S15, the $^1O_2$ spectra obtained from the Fe/Mn-in-CNT-based system was significantly enhanced in D_2O compared with that of H_2O, which provided another solid evidence on the $^1O_2$ generation.

$$O_2 + 2H^+ + 2e^- \rightarrow H_2O_2 \tag{2}$$

$$Mn(IV) + H_2O_2 \rightarrow Mn(III) + O_2^{\bullet-} + 2H^+ \tag{3}$$

$$Mn(III) + H_2O_2 \rightarrow Mn(II) + HO_2^{\bullet} + H^+ \tag{4}$$

$$Fe(III) + H_2O_2 \rightarrow Fe(II) + HO_2^{\bullet}/O_2^{\bullet-} + H^+ \tag{5}$$

$$Fe(III) + HO_2^{\bullet}/O_2^{\bullet-} \rightarrow Fe(II) + H^+ + {}^1O_2 \tag{6}$$

$$Mn(IV)/Mn(III) + HO_2^{\bullet}/O_2^{\bullet-} \rightarrow Mn(III)/Mn(II) + {}^1O_2 + H^+ \tag{7}$$

$$HO_2^{\bullet} \leftrightarrow O_2^{\bullet-} + H^+ \tag{8}$$

$$2HO_2^{\bullet} \rightarrow {}^1O_2 + H_2O_2 \tag{9}$$

$$2O_2^{\bullet-} + 2H_2O \rightarrow {}^1O_2 + H_2O_2 + 2OH^- \tag{10}$$

$$O_2^{\bullet-}/HO_2^{\bullet} + O_2^{\bullet-}/HO_2^{\bullet} \rightarrow {}^1O_2 + H_2O_2 \tag{11}$$

For Fe/Mn-out-CNT-based system, the first step was the generation of H_2O_2 generated *via* ORR at the cathode. Subsequently, Mn(III) on cathode would react with H_2O_2 to produce $HO^{\bullet}$ whilst Fe(II) and Mn(III) recycling might be achieved by a direct electron reduction (Eqs. (12)–(14)), since the standard redox potential of Fe(III)/Fe(II) is 0.77 V *vs* NHE [44] and that of Mn(IV)/Mn(III) is 0.95 V *vs* NHE [45]. The generated Fe(II) could further react with H_2O_2 to form Fe(III) and $HO^{\bullet}$ (Eqs. (15)-(16)). The synergistic effect of Fe and Mn species would result in the recirculation of Fe(III)/Fe(II) and Mn(IV)/Mn(III)/(II) pairs (Eqs. (17)–(18)), and catalyze the conversion of H_2O_2 to $HO^{\bullet}$ (Eq. (19)).

$$Mn(III) + H_2O_2 \rightarrow Mn(IV) + OH^- + HO^{\bullet} \tag{12}$$

$$Fe(III) + e^- \rightarrow Fe(II) \tag{13}$$

$$Mn(IV) + e^- \rightarrow Mn(III) \tag{14}$$

$$Mn(III) + Fe(III) \rightarrow Mn(IV) + Fe(II) \tag{15}$$

$$Fe(II) + H_2O_2 \rightarrow Fe(III) + OH^- + HO^{\bullet} \tag{16}$$

$$Fe(II) + Mn(III) \rightarrow Fe(III) + Mn(II) \tag{17}$$

$$Fe(II) + Mn(IV) \rightarrow Fe(III) + Mn(III) \tag{18}$$

$$Mn(II) + H_2O_2 \rightarrow Mn(III) + OH^- + HO^{\bullet} \tag{19}$$

3.3.3. DFT calculations

DFT calculations were conducted to further elucidate the underlying mechanism of the Fe/Mn-in-CNT-based system. Fig. S16 showed the optimized configurations for H_2O_2 adsorption on the Fe atom and the Mn atom for Fe/Mn-out-CNT and Fe/Mn-in-CNT, respectively. For Fe/Mn-out-CNT, poor H_2O_2 adsorption was observed with E_{ads} of −0.158 eV and −0.313 eV on the Fe and Mn sites, respectively
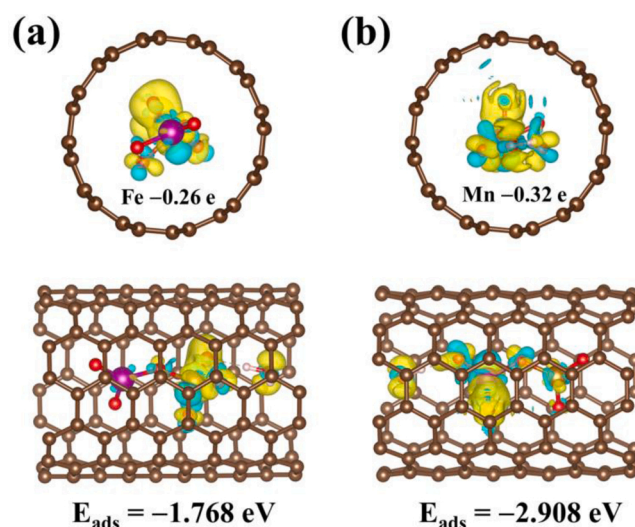

Fig. 7. The DFT-optimized geometries and corresponding charge density difference analysis for (a) Fe/Mn-in-CNT-Fe and (b) Fe/Mn-in-CNT-Mn. Yellow and blue areas represent the increase and reduction of charge density, respectively (Fe: yellow, Mn: purple, H: white, O: red, C: brown).

(Fig. S16a). The weak H_2O_2 adsorption on the Fe/Mn-out-CNT explained the poor decomposition of H_2O_2. Noticeably, the strong Fe/Mn interaction and nanoconfinement effect enabled the O-O bond of H_2O_2 rapidly break after adsorption on the Fe or Mn sites for the Fe/Mn-in-CNT (Fig. S16b). The free energy for the adsorption of H_2O_2 by the Fe and Mn sites was calculated to be −1.768 eV and −2.908 eV, indicating that the nanoconfined spaces within CNT could significantly enhance the E_{ads} of H_2O_2 and the $^1O_2$ yields, facilitating the nanoconfined catalytic performance [46]. Besides, to quantify the electronic density of Fe or Mn atom of Fe/Mn-in-CNT as well as the charge transfer between H_2O_2 and Fe/Mn-in-CNT, the charge density distribution was investigated based on the Bader charge method *via* DFT calculations [47]. The Bader charge of Fe and Mn in the Fe/Mn-in-CNT before reaction was 6.70 e and 5.63 e, whereas that after H_2O_2 adsorption was 6.44 e and 5.31 e (Fig. 7), respectively. Noticeably, the charge transfer number of Mn atom (−0.32 e) in Fe/Mn-in-CNT was more than Fe atom (−0.26 e), indicating that electrons were more likely to transfer from the Mn site of Fe/Mn-in-CNT to H_2O_2 than from Fe site, which would possess higher changer transfer performance during the H_2O_2 activation process [6]. The results verified that the Mn-based Fenton-like oxidation dominated the main catalytic degradation process in Fe/Mn-in-CNT-based system. Overall, the DFT results were good consistent with the experimental findings.

3.4. BPA degradation pathways and intermediate toxicity evaluation

BPA degradation products were identified by the HPLC-MS technique (Fig. S17). Under the ESI− mode, seven dominant substances were detected in the confined electro-Fenton system and two possible BPA degradation pathways were proposed (Fig. 8a). In pathway I, BPA was initiated by attack of methyl group by $^1O_2$, resulting in the formation of demethylation product P1. Then, P2 could be obtained by dephenolization reaction. Pathway II was initiated by $^1O_2$ oxidation of the benzene ring moiety, resulting in the formation of P3 by dephenolization of BPA, and hydroxyacetophenone (P4) could be obtained by further oxidative demethylation. With further ring-opening processes, these above products were further decomposed into smaller intermediates (*e.g.*, P5, P6, and P7) and or even mineralized into CO_2 and H_2O.

To assess the toxicity of degradation intermediates of BPA, the bioconcentration factor and developmental toxicity of BPA and its
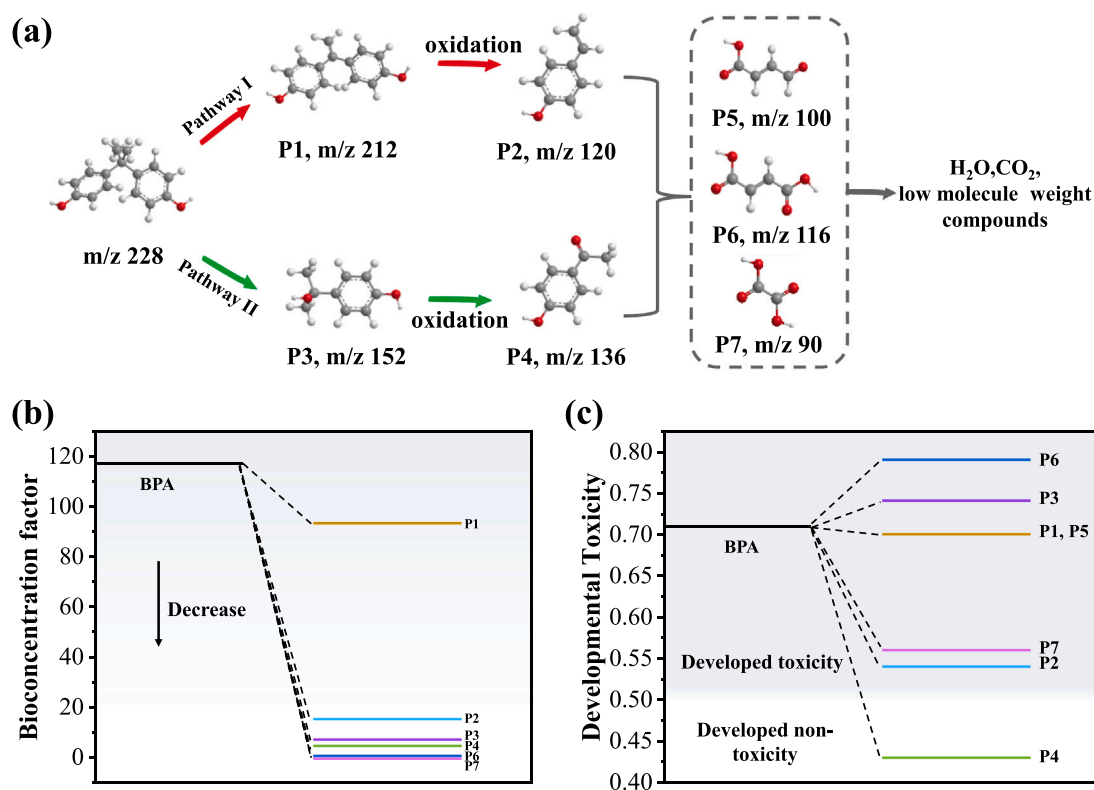
Fig. 8. (a) The proposed pathway of BPA degradation in the Fe/Mn-in-CNT-based system. (b) bioconcentration factor and (c) developmental toxicity of BPA and its degradation intermediates.

degradation intermediates were analyzed using T.E.S.T. software according to QSAR prediction [48]. As displayed in Fig. 8b, the bioconcentration factor of all intermediates showed significantly decreased values than that of BPA, indicating a decreased toxicity of BPA degradation intermediates. In addition, BPA was a "developmental toxicant", while the developmental toxicities of most intermediates were reduced drastically, and product of P4 was even categorized as "developmental non-toxicant" (Fig. 8c). The toxicity attenuation property of the nano-confined electro-Fenton system suggested its potential application in the real water treatment.

3.5. Environmental applications

3.5.1. Effects of operational parameters

The effect of solution pH on BPA degradation by using Fe/Mn-in-CNT filter was displayed in Fig. S18. The BPA degradation remained high efficiency (>85% BPA degradation) across a broad pH range from 3.7 to 9.4 (Table S4). A slight performance decline under alkaline pH could be ascribed to electrostatic repulsion between the negatively charged catalyst and H_2O_2 (Fig. S19). The performance of the Fe/Mn-in-CNT-based system was closely correlated to the applied voltage. As shown in Fig. S20, the BPA removal efficiency gradually increasing from 29.5% to 99.5% with applied voltage decreased from − 1.0 to − 3.0 V, due to an elevated H_2O_2 yield at more negative potentials (Fig. S21). Nevertheless, further decreasing the applied voltage failed to further promoting the BPA degradation kinetics, possible due to the occurrence of other side reactions (Eqs. (20)–(21)).

$$2H_2O_2 \rightarrow 2H_2O + O_2 \tag{20}$$

$$O_2 + 4H^+ + 4e^- \rightarrow 2H_2O \tag{21}$$

Fig. S22 compared the BPA removal performance of the Fe/Mn-in-CNT-based system under batch and flow-through mode as a function of applied voltage. Obviously, the BPA degradation efficiency at a flow

rate of 1.5 mL/min (corresponds to a water flux of 125.2 ± 1.8 L/m^2•h) was significantly higher than that of batch mode. For example, BPA degradation efficiencies were 29.5% and 99.5% under flow-through mode at − 1.0 and − 3.0 V, which was 2.23 and 1.85 times than those obtained in batch, respectively. This phenomenon should be attributed to enhanced mass transfer and improved ROS utilization under the flow-through configuration [49]. The effect of initial concentration on the BPA degradation was also evaluated in the Fe/Mn-in-CNT-based system. As shown in Fig. S23, the BPA degradation efficiency decreased from 99.5% to 70.3% with the increase of BPA initial concentrations from 0.022 to 0.132 mM. The decadent effect could be attributed to the competition of BPA or its degraded intermediates with limited reactive sites on the catalyst in a high BPA concentration solution [50].

The impacts of inorganic anions (CO_3^{2-}, Cl^-, SiO_3^{2-}, and NO_3^-) and natural organic matter (represented by humic acid, HA) on BPA removal were further examined to evaluate the efficacy of the Fe/Mn-in-CNT-based system in complex water matrices. As shown in Fig. S24, a high activity of the catalyst (>90.0% BPA degradation within 90 min) could still be remained. Furthermore, BPA degradation in more complicated water matrices (*e.g.*, tap water, lake water, and WWTP secondary effluent, detailed water characteristics were provided in Table S5) was conducted. As present in Fig. S25, the BPA removal efficiencies still surpassed 85.0% in all these complex water matrices. Thus, the Fe/Mn-in-CNT-based system exhibited excellent performances in degradation of organic contaminants in practical scenarios.

3.5.2. Ionization potential-dependent selective oxidation of organic contaminants

It has been reported that the IP value of the organic compounds can be used as an indicator to reflect their reactivity toward oxidation [38]. Generally, a lower IP would be expected with the presence of electron-donating moieties (*e.g.*, hydroxyl) in organic molecules [18], and *vice versa* for the electron-withdrawing moieties (*e.g.*, nitrophenyl and carboxyl groups) [51]. The efficacy of $^1O_2$-mediated oxidation
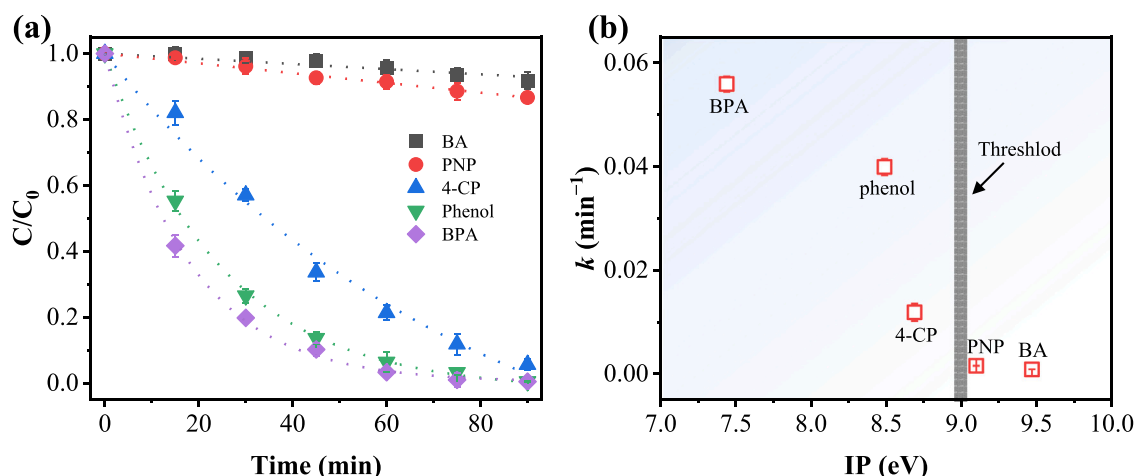
Fig. 9. (a) Selective oxidation of organic compounds in the Fe/Mn-in-CNT-based system and (b) relationship between IP values and degradation kinetics of different organic compounds. Experimental conditions: $[BA]_0 = [PNP]_0 = [4\text{-}CP]_0 = [phenol]_0 = [BPA]_0 = 0.022$ mM, $[Na_2SO_4] = 10$ mM, $[DO]_0 = 37.6 \pm 1.2$ mg/L, voltage $= -3.0$ V, $[pH]_0 = 6.8$, and flow rate $= 1.5$ mL/min.

kinetics greatly depended on the electron-donating ability of organics [38], which was closely correlated with the IP value. Thus, the substrate specificity of $^1O_2$ towards BA (IP = 9.47 eV), PNP (IP = 9.1 eV), phenol (IP = 8.49 eV), 4-CP (IP = 8.69 eV), and BPA (IP = 7.44 eV) was investigated (Table S6). Specifically, BA and PNP with electron-withdrawing groups (*i.e.*, carboxyl and nitrophenyl) were less susceptible to degradation, whereas phenol, 4-CP, and BPA with electron-donating groups (*i.e.*, hydroxyl) were more readily to be degraded. As present in Fig. 9a, degradation kinetics of the five aromatic compounds in the nanoconfined electro-Fenton process followed the order of BA (0.001 min^{-1}) < PNP (0.0017 min^{-1}) < 4-CP (0.012 min^{-1}) < phenol (0.041 min^{-1}) < BPA (0.056 min^{-1}). In addition, the correlation between IP values and corresponding degradation kinetics was established. As illustrated in Fig. 9b, the degradation rate constants of organic compounds were negatively correlated to their IP value, suggesting that the electron-donating ability of organics notably affected the preferential reaction of the Fe/Mn-in-CNT-based system. These results demonstrated the great effectiveness of the proposed nanoconfined electro-Fenton technology to selectively degrade electron-donating compounds in real wastewater containing complicated components.

3.5.3. System stability and energy consumption

Heterogeneous AOPs usually require robust catalysts for the practical wastewater treatments [37]. Thus, the stability of the Fe/Mn-in-CNT-based system was further examined. As shown in Fig. S26, only a marginal decline in BPA removal efficiency were experienced after five continuous running cycles, demonstrating the outstanding stability of Fe/Mn-in-CNT filter in catalytic oxidation. Since the cumulative BPA degradation products might obscure these active sites or react with $^1O_2$, the exhausted filter was washed with ethanol to restored its catalytic activity, as evidenced by the recovered BPA degradation efficiency for another five running cycles. This demonstrated that the outer carbon layer protection could suppress Fe and Mn leaching into the reaction and ensure the stability of the catalyst.

The electric energy consumption was a critical indicator to evaluate the economic efficiency of the Fe/Mn-in-CNT-based system in practical application. The electric energy consumption per volume treated for BPA removal in Fe/Mn-in-CNT-based system was calculated to be 0.18 kWh/m^3 at an applied voltage of -3.0 V with a corresponding current of 0.002 A, which was comparable to several state-of-the-art electro-Fenton systems (Table S7). Overall, the Fe/Mn-in-CNT-based system provided a promising process for cost-effective removal of organic contaminants in wastewater treatment applications.

4. Conclusions

In this study, the degradation of BPA using a Fe/Mn-in-CNT filter as the cathode were systematically investigated in a flow-through electro-Fenton system. Benefited from the synergistic effect of confined Fe/Mn, CNT, and electric field, the performance of Fe/Mn-in-CNT filter was significantly enhanced. DFT calculations suggested that H_2O_2 could be rapidly decomposed under nanoconfined environment. Additionally, the space-limited structure of CNT protected the active Fe/Mn oxides from leaching into the aqueous solution environment, thus ensuring an excellent stability and reusability. Experimental results revealed that the mechanism of the enhanced catalytic performance originated from a $^1O_2$-based nonradical pathway. Importantly, the electrophilic characteristics of $^1O_2$ were conducive to efficient degradation of organic pollutants with electron-donating moieties (as reflected by IP), which minimized wasteful consumption of $^1O_2$ by background water ingredients. The current work will provide an economical and promising technology for eliminating organic contaminants in actual water treatment with excellent degradation activity, selectivity, and good environmental robustness.

CRediT authorship contribution statement

Dongli Guo: Data curation, Methodology, Investigation, Writing – original draft. **Yi Wang:** Writing – review & editing, Project administration, Resources. **Ping Lu:** Characterizations. **Jie Liu:** Discussion, Resources. **Yanbiao Liu:** Conceptualization, Writing – review & editing, Supervision.

Declaration of Competing Interest

The authors declare that they have no known competing financial interests or personal relationships that could have appeared to influence the work reported in this paper.

Data availability

Data will be made available on request.

Acknowledgements

M201912902).

Appendix A. Supporting information

Supplementary data associated with this article can be found in the online version at doi:10.1016/j.apcatb.2023.122538.

References

[1] V.I. Parvulescu, F. Epron, H. Garcia, P. Granger, Chem. Rev. 122 (2022) 2981–3121.
[2] J.W. Xu, X.L. Zheng, Z.P. Feng, Z.Y. Lu, Z.W. Zhang, W. Huang, Y.B. Li, D. Vuckovic, Y.Q. Li, S. Dai, G.X. Chen, K.C. Wang, H.S. Wang, J.K. Chen, W. Mitch, Y. Cui, Nat. Sustain. 4 (2021) 233–241.
[3] Y.F. Ren, W.T. Zheng, N. Goswami, Y.B. Liu, Environ. Funct. Mater. 1 (2022) 10–20.
[4] M.H. Li, S.J. You, X.G. Duan, Y.B. Liu, Appl. Catal., B 312 (2022) 121419.
[5] W.T. Zheng, Y.B. Liu, F.Q. Liu, Y. Wang, N.Q. Ren, S.J. You, Water Res 223 (2022), 118994.
[6] L.L. Cui, X.Y. Zhao, H.J. Xie, Z.H. Zhang, ACS Catal. 12 (2022) 13334–13348.
[7] S.O. Ganiyu, M.H. Zhou, C.A. Martinez-Huitle, Appl. Catal., B 235 (2018) 103–129.
[8] E. Brillas, Sci. Total Environ. 819 (2022), 153102.
[9] S. Zhang, M. Sun, T. Hedtke, A. Deshmukh, X. Zhou, S. Weon, M. Elimelech, J. H. Kim, Environ. Sci. Technol. 54 (2020) 10868–10875.
[10] J.S. Qian, X. Gao, B.C. Pan, Environ. Sci. Technol. 54 (2020) 8509–8526.
[11] Y. Chen, G. Zhang, H.J. Liu, J.H. Qu, Angew. Chem. Int. Ed. 58 (2019) 8134–8138.
[12] S. Zhang, T. Hedtke, X.C. Zhou, M. Elimelech, J.H. Kim, ACS EST Eng. 1 (2021) 706–724.
[13] D.L. Guo, Y.B. Liu, H.D. Ji, C.C. Wang, B. Chen, C.S. Shen, F. Li, Y.X. Wang, P. Lu, W. Liu, Environ. Sci. Technol. 55 (2021) 4045–4053.
[14] M. Zhang, C.M. Xiao, X. Yan, S.S. Chen, C.H. Wang, R. Luo, J.W. Qi, X.Y. Sun, L. J. Wang, J.S. Li, Environ. Sci. Technol. 54 (2020) 10289–10300.
[15] P. Su, W.Y. Fu, X.D. Du, G. Song, M.H. Zhou, Chem. Eng. J. 420 (2021) 129446.
[16] Z.C. Yang, J.S. Qian, A.Q. Yu, B.C. Pan, Proc. Natl. Acad. Sci. USA 116 (2019) 6659–6664.
[17] D.L. Guo, S.T. Jiang, L.M. Jin, K. Huang, P. Lu, Y.B. Liu, J. Mater. Chem. A 10 (2022) 15981–15989.
[18] P.J. Duan, X. Xu, K.Y. Guo, Q.Y. Yue, B.Y. Gao, Appl. Catal., B 316 (2022) 121695.
[19] Z. Wang, C.C. Meng, W. Zhang, S.Z. Zhang, B. Yang, Z.H. Zhang, Sci. Total Environ. 814 (2022), 152698.
[20] Y.M. Zhao, M. Sun, X.X. Wang, C. Wang, D.W. Lu, W. Ma, S.A. Kube, J. Ma, M. Elimelech, Nat. Commun. 11 (2020) 6228–6237.
[21] A.D. Bokare, W. Choi, J. Hazard. Mater. 275 (2014) 121–135.
[22] Y.H. Lin, P.F. Huo, F. Li, X.M. Chen, L.Y. Yang, Y. Jiang, Y.F. Zhang, B.J. Ni, M. H. Zhou, Chem. Eng. J. 450 (2022) 137948.
[23] L.M. Jin, S.J. You, X.G. Duan, Y. Yao, J.M. Yang, Y.B. Liu, J. Hazard. Mater. 423 (2021) 127111.
[24] H. Xia, Z. Zhang, J. Liu, Y. Deng, D.X. Zhang, P.Y. Du, S.T. Zhang, X.Q. Lu, Appl. Catal., B 259 (2019) 118058.
[25] X.L. Pan, Z.L. Fan, W. Chen, Y.J. Ding, H.Y. Luo, X.H. Bao, Nat. Mater. 6 (2007) 507–511.
[26] G. Gao, C.D. Vecitis, Environ. Sci. Technol. 45 (2011) 9726–9734.
[27] C.D. Vecitis, M.H. Schnoor, M.S. Rahaman, J.D. Schiffman, M. Elimelech, Environ. Sci. Technol. 45 (2011) 3672–3679.
[28] Y.Q. Huang, C.K. Wong, J.S. Zheng, H. Bouwman, R. Barra, B. Wahlstrom, L. Neretin, M.H. Wong, Environ. Int. 42 (2012) 91–99.
[29] Y. Kurata, Y. Ono, Y. Ono, J. Mater. Cycles Waste Manag. 10 (2008) 144–152.
[30] J.P. Perdew, K. Burke, M. Ernzerhof, Phys. Rev. Lett. 77 (1996) 3865–3868.
[31] G. Kresse, D. Joubert, Phys. Rev. B 59 (1999) 1758–1775.
[32] T. Trang Nguyen, P. Serp, ChemCatChem 5 (2013) 3595–3603.
[33] W.J. Yang, K.L. Sun, J. Wan, Y.-A. Ma, J.Q. Liu, B.C. Zhu, L. Liu, F. Fu, Appl. Catal., B 320 (2023), 121978.
[34] L. Li, C. Lai, F.L. Huang, M. Cheng, G.M. Zeng, D.L. Huang, B.S. Li, S.Y. Liu, M. M. Zhang, L. Qin, M.F. Li, J.F. He, Y.J. Zhang, L. Chen, Water Res. 160 (2019) 238–248.
[35] A. Ramírez, P. Hillebrand, D. Stellmach, M.M. May, P. Bogdanoff, S. Fiechter, J. Phys. Chem. C. 118 (2014) 14073–14081.
[36] S.L. Wang, S.Z. Pei, J.N. Zhang, J.Q. Huang, S.J. You, Water Res. 218 (2022), 118454.
[37] J. Kang, L. Zhou, X.G. Duan, H.Q. Sun, Z. Ao, S.B. Wang, Matter 1 (2019) 745–758.
[38] S.S. Zhu, X.J. Li, J. Kang, X.G. Duan, S.B. Wang, Environ. Sci. Technol. 53 (2019) 307–315.
[39] Y.Y. Jiang, P.J. Ni, C.X. Chen, Y.Z. Lu, P. Yang, B. Kong, A. Fisher, X. Wang, Adv. Energy Mater. 8 (2018), 1801909.
[40] M.J. Huang, S.S. Peng, W. Xiang, C. Wang, X.H. Wu, J. Mao, T. Zhou, Chem. Eng. J. 429 (2022), 132372.
[41] M.K. Panjwani, Q. Wang, Y.M. Ma, Y.X. Lin, F. Xiao, S.X. Yang, Environ. Sci.: Nano 8 (2021) 2204–2213.
[42] Q.Y. Yi, J.H. Ji, B. Shen, C.C. Dong, J. Liu, J.L. Zhang, M.Y. Xing, Environ. Sci. Technol. 53 (2019) 9725–9733.
[43] Y.W. Gao, Z.H. Chen, Y. Zhu, T. Li, C. Hu, Environ. Sci. Technol. 54 (2020) 1232–1241.
[44] J.M. Hudson, G.W. Luther, Y.P. Chin, Environ. Sci. Technol. 56 (2022) 9123–9132.
[45] S. Ndayiragije, Y.F. Zhang, Y.Q. Zhou, Z. Song, N. Wang, T. Majima, L.H. Zhu, Appl. Catal., B 307 (2022) 121168.
[46] D.L. Guo, Y. Yao, S.J. You, L.M. Jin, P. Lu, Y.B. Liu, Appl. Catal., B 309 (2022), 121289.
[47] P.P. Zhang, Y.Y. Yang, X.G. Duan, Y.J. Liu, S.B. Wang, ACS Catal. 11 (2021) 11129–11159.
[48] C.Y. Dang, F.B. Sun, H. Jiang, T.B. Huang, W. Liu, X.M. Chen, H.D. Ji, J. Hazard. Mater. 400 (2020), 123225.
[49] L.L. Cui, M.M. Sun, Z.H. Zhang, Chem. Eng. J. 450 (2022), 138263.
[50] C.Q. Zhu, S.F. Zhao, Z.W. Fan, H.D. Wu, F.Q. Liu, Z.X. Chen, A.M. Li, Adv. Funct. Mater. 30 (2020), 2003947.
[51] Z.H. Xie, C.S. He, H.Y. Zhou, L.L. Li, Y. Liu, Y. Du, W. Liu, Y. Mu, B. Lai, Environ. Sci. Technol. 56 (2022) 8784–8795.